Aligned TiO2 Nanotube Arrays As Durable Lithium-Ion Battery Negative Electrodes

7 AUTHORS, INCLUDING:

Juchuan (JC) Li
Lawrence Berkeley National Laboratory
31 PUBLICATIONS   432 CITATIONS

Navaladian Subramanian
24 PUBLICATIONS   292 CITATIONS

Stephen E Rankin
University of Kentucky
124 PUBLICATIONS   1,510 CITATIONS

Fuqian Yang
University of Kentucky
259 PUBLICATIONS   2,683 CITATIONS

Aligned TiO₂ Nanotube Arrays As Durable Lithium-Ion Battery Negative Electrodes

Qing Liu Wu,[†,‡] Juchuan Li,[†,⊥] Rutooj D. Deshpande,[†,§] Navaladian Subramanian,[∥] Stephen E. Rankin,* Fuqian Yang,* and Yang-Tse Cheng*

Chemical and Materials Engineering Department, University of Kentucky, 177 F. P. Anderson Tower, Lexington, Kentucky 40506-0046, United States

Ⓢ Supporting Information

ABSTRACT: Vertically aligned amorphous titania (TiO₂) nanotubes are produced by anodizing Ti foils at various applied potentials in a neutral electrolyte solution containing fluoride ions. Pore size and wall thickness are tuned in the range from 30 to 70 nm and 17 to 35 nm, respectively, by adjusting the applied potential, in addition to tuning the tube length from 355 to 550 nm. Utilizing all of these films as negative electrode materials in lithium-ion batteries delivers stable capacities of 130−230 mAh g⁻¹ and 520−880 mAh cm⁻³ up to 200 cycles. Microstructural analysis shows that there is no structural change or mechanical degradation in the active material, and the amorphous active material maintains good contact with the substrate/current collector. A continuum elasticity model for the tubular geometry is presented to understand the diffusion-induced stresses, fracture tendency, and stability in TiO₂ nanotubes. Modeling results indicate that the fracture tendencies of nanotubes with the dimensions in this work are very small; stable reversible capacity retention results from the high ratio of inner to outer diameter of the tubes. In other words, tubes with thinner walls more easily accommodate expansion or contraction during the lithiation/delithiation process. A guideline for designing lithium-ion battery nanotube electrodes is given such that under specific conditions the fracture tendency is small and volumetric charge density is high.
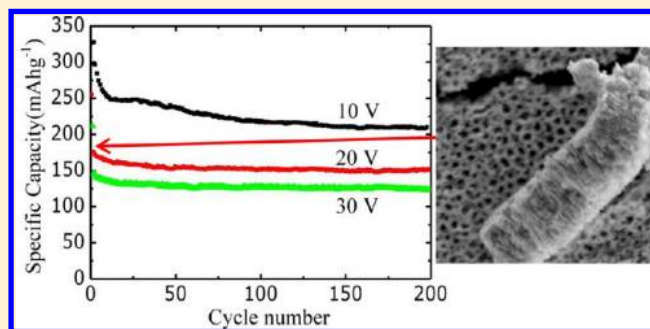
1. INTRODUCTION

Lithium-ion batteries (LIBs) are among the most promising technologies for stationary energy storage where safety, stable cycle life, and low cost are major concerns and the gravimetric and volumetric energy densities of electrodes are less important.[1] Many advanced LIB anode materials, including Si, Ge, and Sn, have the advantage of higher capacity than graphite, which is currently used in commercial production of these batteries.[2] However, their applications are limited in stationary energy storage because at low operating voltage (below 1 V vs Li/Li⁺) the lithium salt-based liquid electrolyte decomposes, leading to release of gases and potential buildup of pressure in the cells, and because of formation of an unstable solid electrolyte interface (SEI) on the electrode surface.[3,4] Thus, negative electrode materials with high discharging potentials in which the electrolyte solution is stable, such as the lithium titanate (Li₄Ti₅O₁₂)/titania (TiO₂) system, are of interest for stationary energy applications. Compared with Sn, Si, or graphite, the theoretical capacity of TiO₂ is lower but the overall safety of the cells is greatly improved.

TiO₂ delivers a high discharge voltage plateau of about 1.7 V,[5] stable cycling performance,[6] and small volume expansion (~3%) during lithiation/delithiation.[7] However, one significant disadvantage of titania is that it has poor lithium ionic and electrical conductivities, which limit the charge/discharge rate

in bulk titania.[6] It has been well established that the lithium intercalation activity and cycling stability depend on the morphology of electrode materials, and these properties of titania-based electrodes have improved dramatically as materials with nanoscale features have been developed.[8,9] Therefore, numerous studies have been reported aimed at reducing lithium diffusion length by fabrication of nanostructured TiO₂ materials, such as nanosized anatase titania,[10] TiO₂−B nanowires,[11] and mesoporous rutile.[6]

Well-oriented nanotube arrays provide a promising morphology for LIB negative electrodes because of their high accessible surface area for lithium introduction into the solid matrix, the short Li⁺ diffusion path length in the solid phase, and the possibility that the tubular structure can accommodate the expansion and contraction occurring during the lithium-ion insertion and removal processes. In fact, the latter advantage of titania nanotube arrays as anodes for lithium-ion batteries has been utilized already by several researchers. Lindsay et al. reported the use of anodized titanium foils as negative electrodes for LIBs[12] but found considerable amounts of damage or loss of capacity in thick films because they had only sparse or no porosity.[13] In contrast, other groups reported good

retention of capacity (over 90%) for between 50 and 100 cycles.[5,14] The best durability reported in titania nanotube-based lithium-ion batteries was recently reported by Wei et al. for anatase arrays with an average pore diameter of 50 nm and wall thickness of 25 nm, which retained 96.4% of their capacity over 140 charge/discharge cycles.[15] However, capacity retention dropped quickly to only 53% with 100 nm diameter, 40 nm thick tubes, and further decay of capacity was observed for larger diameter/thickness combinations.[15] From these results, a pattern emerges of good capacity retention (>90%) for walls under 40 nm in thickness, irrespective of pore diameter. However, the effects of the ratio of the inner to the outer diameter of the tubes on the durability of titania nanotube arrays electrodes has not been directly elucidated in the above reports, and the reasons for capacity retention or loss have not been explained.

Here, we fabricate aligned TiO_2 nanotubes with controlled pore size and wall thickness by anodizing pure Ti foils in a neutral fluoride solution comprising $(NH_4)_2SO_4$ and NH_4F as the electrolyte and use these nanotube arrays as examples to investigate structural and capacity stability during battery cycling. The anodic oxidation technique is widely used to produce titania nanotubes due to its capability of controlling pore size, length of tubes, and uniformity over large areas at low cost.[16] Use of neutral fluoride solutions allows fabrication of TiO_2 nanotubes with thin walls by reducing the dissolution rate of oxide layers.[17,18] Furthermore, as we will show below, these anodization conditions give tubes with amorphous walls; amorphous TiO_2 has higher capacity for lithium ions than anatase because of the large density of defects in the disordered structure.[14,19] The electrochemical performance of the titania nanotube arrays as LIB electrodes is measured over 200 galvanostatic cycles, and excellent capacity retention is observed for titania tubes of selected dimensions. Recently, Cheng and Verbrugge[20−23] and Yang et al.[24,25] developed mathematical models to elucidate the roles of diffusion-induced stresses, battery operating conditions, and surface properties of nanoscaled electrodes in overall stress development and potential for fracture. Following Cheng and Verbrugge,[20−23] we propose a theoretical model of diffusion-induced stress (DISs) for tubular electrode element, which explains the good capacity retention of TiO_2 nanotubes in this work and also provides guidelines for designing TiO_2 nanotubes with high capacity and stable cycling performance.

2. EXPERIMENTAL SECTION

2.1. Preparation of TiO₂ Nanotube Arrays. Pure Ti foils (99.6%, Strem Chemicals) with a thickness of 0.025 mm were used to prepare TiO_2 nanotube electrodes. Electrochemical anodization was carried out at room temperature in a homemade cell with a two-electrode configuration. A dc power supply (model 3603D, Spence Tek) was used to provide a constant potential during the anodization process. Ti foils with an exposed area of 3.14 cm² acted as the anodes, and a Pt foil with an area of 2.25 cm² was used as the cathode. The distance between the anode and the cathode was maintained at 7 cm. Electrolyte was a solution of 0.5 wt % NH_4F (reagent grade, MP biomedicals) dissolved in 1 M $(NH_4)_2SO_3$ (GR grade, EMD chemicals). Potential was increased from 0 V to the final potentials at a ramp rate of 200 mV s⁻¹ and then held at designated potentials of 5, 10, 20, and 30 V for 2 h. After anodization, samples were washed with deionized water and

dried in vacuum at 110 °C overnight before electrochemical measurements.

2.2. Electrochemical Characterization. The electrochemical performance of TiO_2 nanotube arrays was tested in CR2025 coin cells using the anodized titania foils as the working electrodes (WE) and pure Li metal foils as the counter electrodes (CE). Cells were fabricated in an Ar-filled glovebox (MBraun), where the oxygen and moisture levels were below 0.1 ppm. Electrolyte was 1 M $LiPF_6$ salt dissolved in an equal-volume mixture of ethylene carbonate and dimethyl carbonate (Novolyte). Coin cells were galvanostatically cycled between 1.0 and 2.7 V at a rate of C/3, which was controlled by a multichannel potentiostat (VMP3, Bio-Logic). This corresponds to 3 h charge/discharge cycles at a current of roughly 10 μA (see Appendix B, Supporting Information for more information).

2.3. Materials Characterization. X-ray diffraction (XRD) analysis using Cu Kα (λ = 1.5406 Å) radiation was employed to determine the titania film crystal structure. Measurements were conducted directly on the thin films in Bragg−Brentano geometry using a Bruker D8 Advance diffractometer. For plan-view imaging of the pore accessibility, films were left intact and the conductivity was increased by coating the samples with a layer of Au/Pt alloy using a sputtering process (EMSCOPE SC400) for 1 min. Scanning electron microscope (SEM) images were subsequently collected with a Hitachi S-4300 microscope at 3 kV. To observe the edges of fractured films, samples were mechanically bent before mounting onto the stage. For sample observation after cycling, cells were disassembled and the anodized titania (WE) was washed with dimethyl carbonate (99.9%, Alfa Aesar) to remove residual electrolyte salt.

3. RESULTS AND DISCUSSION

3.1. Titania Nanotube Arrays Prepared by Anodization. After anodization, refraction of visible light to give regions of different color, including green and red, is observed in anodized regions on Ti foils under visual inspection. To determine the crystallinity of the titania films, XRD measurements were performed on the Ti foil before and after anodization. Representative results with the anodization potential set at 5 and 20 V are shown in Figure 1. All observed
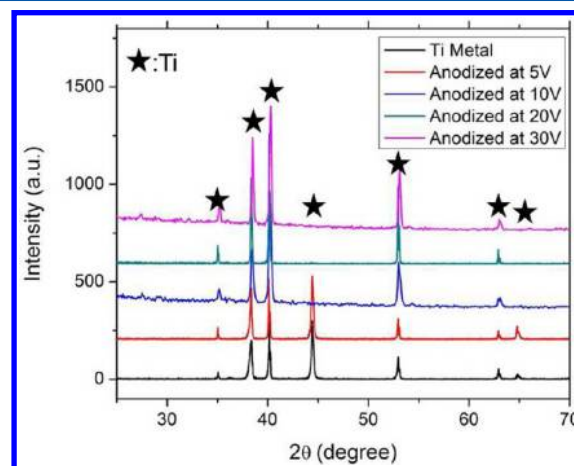

Figure 1. XRD patterns of pristine Ti metal foil and after anodization at 5, 10, 20, or 30 V for 2 h. All reflections indicated are assigned to Ti metal.

diffraction peaks can be assigned to Ti metal, and no characteristic diffraction peaks ascribed to crystalline titania including anatase, rutile, or brookite are observed. This implies that the resulting products after anodizing Ti foil are X-ray amorphous titania regardless of the applied potentials, which is consistent with reports by other researchers that only amorphous titania can be produced via anodization without high-temperature annealing.[5,14,15]

Although it has no influence on the crystallinity, the anodization potential strongly affects the morphology of titania, which is illustrated in plan-view SEM images in Figure 2. When the anodization potential is above 10 V under the conditions employed, uniform and vertically aligned titania nanotubes are observed with pores accessible to the surface (Figure 2b, 2c, and 2d). In contrast to the appearance of the surface at high anodization voltages, when the anodization potential is 5 V, only a porous layer of oxidized material without tubular features is observed in the anodized region (Figure 2a). At intermediate voltages (10 and 20 V), the surface is uniform and smooth looking, but the surface of the anodized region obtained at 30 V is rougher and less uniform. Convex features are observed at the top surface of the titania nanotube walls, which suggests that the top surfaces of nanotubes are partially eroded at the high applied potential. Views of the edges of fractured films (Figure 3) indicate that all nanotube arrays consist mainly of straight cylindrical tubes aligned vertical to the substrate foil. In contrast to the top surface, a domelike structure is observed at the bottom surface of the tube arrays. This is a thin oxidized layer separating the porous layer from the metal substrate, which is so called a barrier layer, and has been reported by other researchers.[16]

The length of the tubes is measured from these fractured film images, and the diameters and wall thicknesses are estimated by averaging 70−100 tubes from the SEM images in Figure 2. The diameters and wall thicknesses of titania nanotubes obtained as a function of anodization potential are shown in Figure 4. The average pore diameters of the tubes increases from about 30 to about 70 nm as the anodization potential is increased from 10 to 20 V. However, the pore diameter does not change significantly when the anodization potential is further increased to 30 V. The higher anodization potential significantly expands the walls of the nanotubes, which increase in thickness from about 17 nm at 10 V to 19 nm at 20 V and to 35 nm at 30 V. The effect of the applied potential on the length of tubes is not monotonic and probably reflects a trade off between the rate of formation of tubes and the rate of etching away material. The tubes are 350 nm long at 10 V, and the length increases to 550 nm at 20 V, while the length decreases again to 350 nm as the anodization voltage increases to 30 V, which is an indication of erosion.

The influence of applied potential on the porous architecture of anodized titania nanotubes can be interpreted by the well-accepted field-enhanced dissolution mechanism,[16,17,26] which classifies the formation pathway of titania nanotubes into several stages, including formation of the initial oxide layer, dissolution of the layer in water in the presence of fluoride ions with the assistance of the electric field, and removal of Ti^{4+} ions out of the unanodized region under electric field.[27,28] Growth of pores is a result of the different current intensities between the top surface of the metal and the bottom of the pores. Compared with the top surface of the oxide layer, the higher current intensity at the bottom of pores drives titanium oxide dissolution at a higher rate, leading to continuous growth of
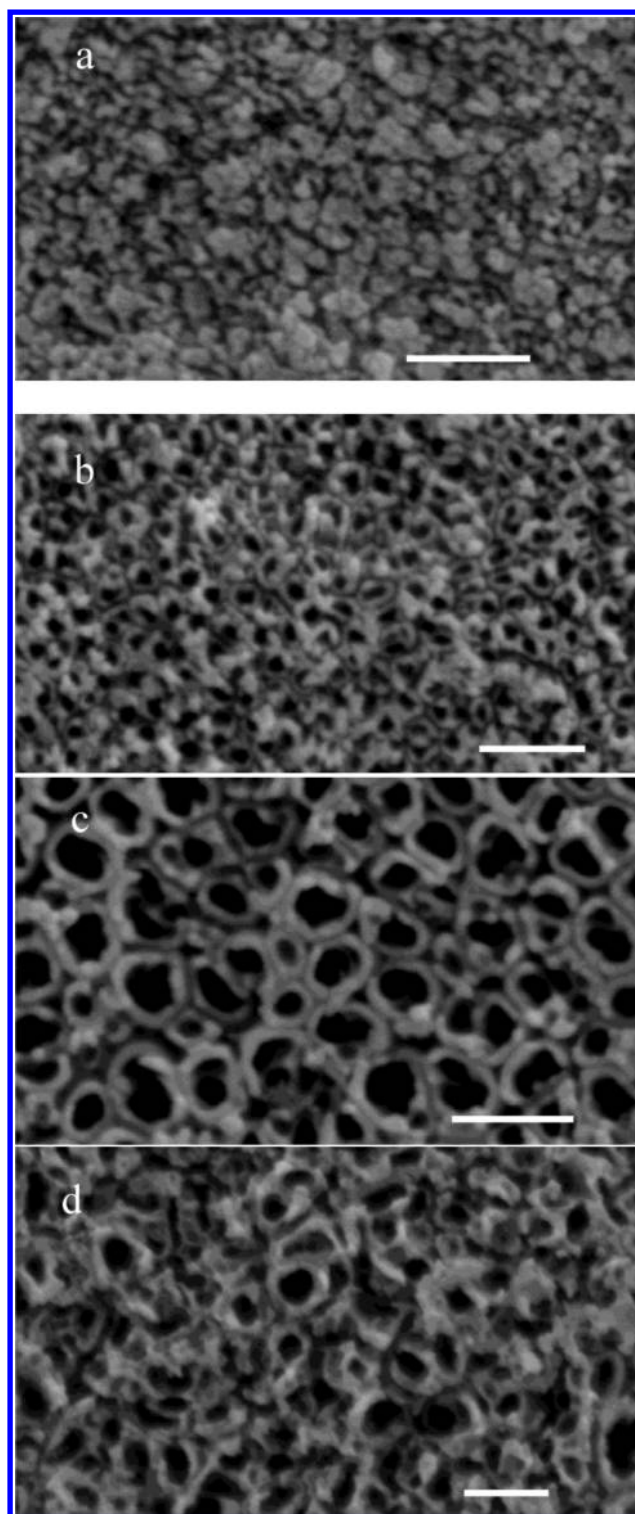

Figure 2. Plan-view SEM images of TiO_2 nanotubes after anodization for 2 h. Applied anodization voltages are (a) 5, (b) 10, (c) 20, and (d) 30 V. Scale bars are 250 nm in all figures.

pores into the metal. Growth of tubes stops when a balance of etching rate between the top and the bottom of tubes is reached.[26,29] Therefore, with a higher anodization potential, tubes with longer length could be achieved (Figure 3a and 3b). The enhancement of pore size with higher potentials (Figure 4) can also be understood by this formation mechanism as being a result of an increase in the spacing of heterogeneities in the
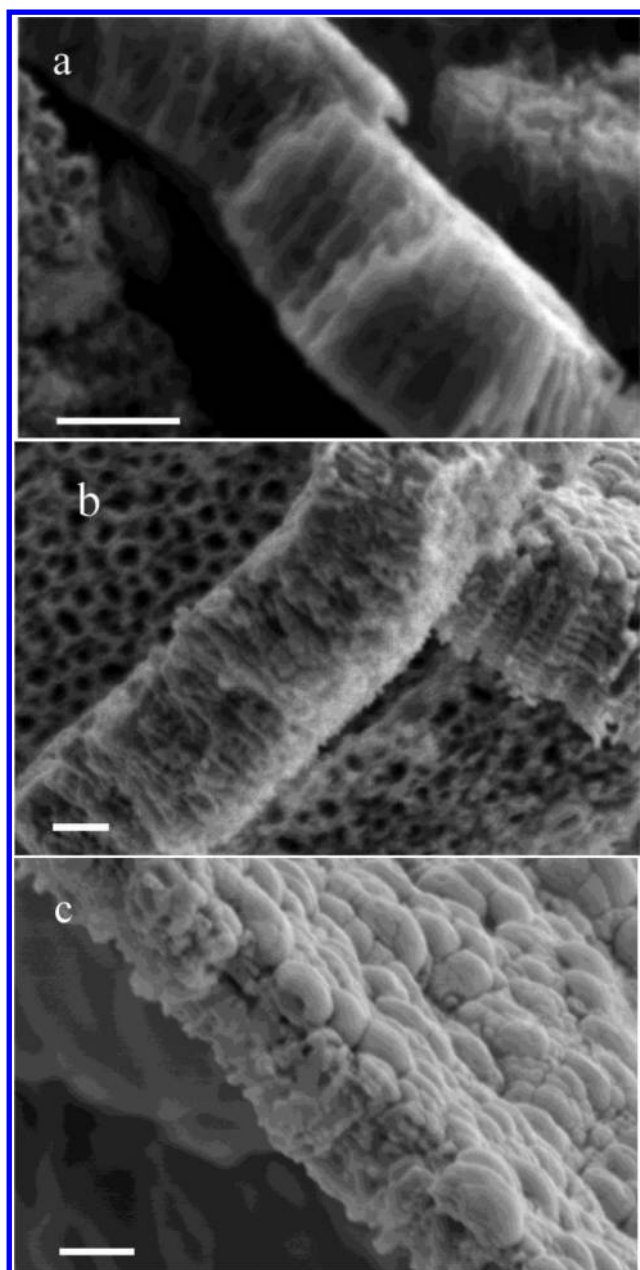
Figure 4. Dependence of pore diameter and wall thickness of TiO_2 nanotubes on anodization potential.

vs potential profiles are shown in Figure 5. In contrast with anatase titania electrodes which usually exhibit a sharp peak

Figure 5. Typical differential capacity vs potential plots of lithiated/delithiated anodized TiO_2 nanotubes obtained with different applied potentials. Applied potential to prepare electrode materials is denoted as 10, 20, and 30 V.

Figure 3. SEM images of the edges of fractured TiO_2 nanotubes after anodization for 2 h. Applied anodization voltages are (a) 10, (b) 20, and (c) 30 V. Scales bars are 250 nm in all images.

lateral distribution of the electric field as the voltage increases. Furthermore, more current distributed in the pore rather than in the wall at higher potential hinders development of pinholes between tubes, finally leading to enhancement of wall thickness with higher potentials (Figure 4). However, pores with much larger diameter will connect with each other, eventually leading to collapse of the nanotubes and a drop of tube length (comparing Figure 2c and 2d). Observation of porous structure instead of tubular features is the result of the failure to etch away titanium ions from metallic areas at an insufficient potential of 5 V (Figure 2a) under the specific solution conditions used in this work.

3.2. Cycling Performance of TiO_2 Nanotubes. The electrochemical performance of the titania nanotubes as LIB electrodes has been examined, and typical differential capacity
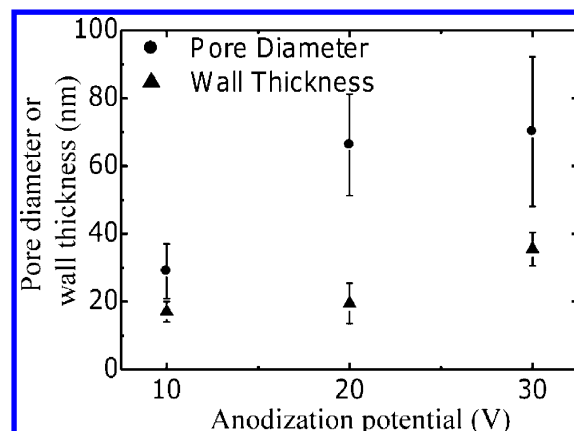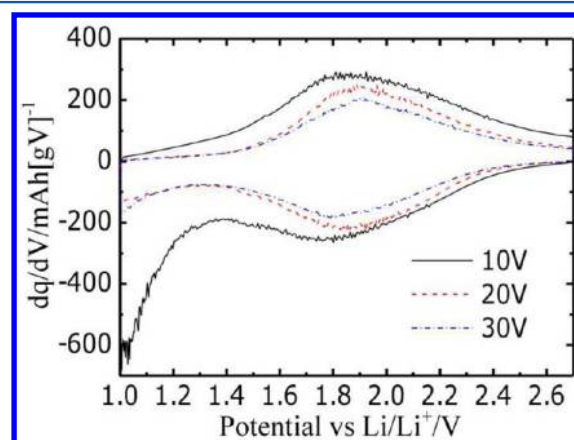
centered near 1.8 V during discharge and 1.9 V during charging corresponding to insertion and extraction of Li^+ from the tetrahedral and octahedral sites of crystalline anatase,[5,6,30−32] derivative curves of all amorphous titania nanotubes obtained at an anodization voltage between 10 and 30 V show only broad humps in the range of 1.4−2.5 V during cycling. This behavior is consistent with earlier reports on the electrochemical behavior of amorphous titania.[5,14] The broad hump for each condition does not change with further cycling, indicating that titania nanotubes remain amorphous during the entire process studied, consistent with XRD observations in Figure 1. The expanded potential range for Li^+ insertion is ascribed to the specific structure of amorphous titania which contains a large amount of disordered structures and defects compared with anatase TiO_2.[14] The disordered structures and defects provide a nonuniform distribution of spaces for insertion of lithium ions during the discharge process, leading to the absence of sharp peaks in the differential charge/discharge curves.

The amorphous titania nanotube electrodes exhibit desirable cycling performances, as shown in Figure 6. The mass of active materials was estimated by measuring the volume of the titania nanotube on each sample and taking the density of the solid
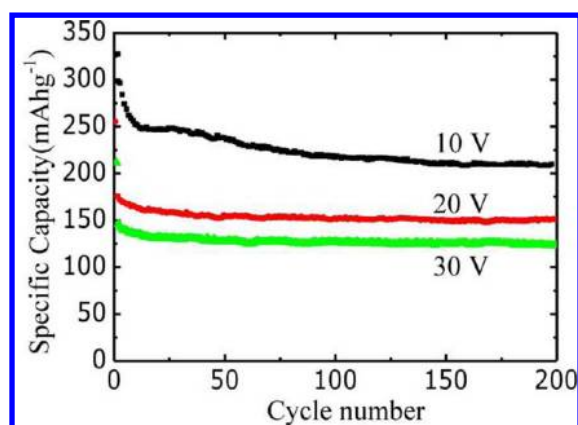
18672

dx.doi.org/10.1021/jp3072266 | J. Phys. Chem. C 2012, 116, 18669−18677

Figure 6. Cycling performance of anodized titania nanotubes obtained with various applied potentials up to 200 cycles at a 1/3 C rate. Applied potential to prepare electrode materials is indicated as 10, 20, and 30 V.

Figure 7. Plan-view SEM images of TiO_2 nanotubes after 200 electrochemical cycles. Applied anodization voltages are (a) 10, (b) 20, and (c) 30 V. Scales bars are 500 nm in all images.

phase to be 3.84 g cm^{-3} in the calculation. As indicated by Figure 6, all samples prepared at different anodization voltages exhibit excellent capacity retention upon cycling at 1/3 C rate after the initial capacity drop. After 200 cycles, the discharge capacity remains as high as 130 mAh g^{-1} for the sample derived at 30 V and increases to 150 and 210 mAh g^{-1} when the applied anodization voltage decreases to 20 and 10 V, respectively. The total capacity fading is less than 6% between the 10th and 200th cycle for samples anodized 20 and 30 V and is 12.5% for the sample anodized at 10 V. Even for this sample fabricated at 10 V the capacity fading is as low as 4.5% during the interval from the 100th to the 200th cycle, while it is 9% during the interval from the 10th to the 100th cycle. Figure 7 shows the morphology of titania nanotubes after 200 electrochemical cycles. There is no visible crack or other damage on the surface of the films, and tubular structures are well preserved after 200 cycles and maintain contact with the Ti metal substrates. Compared with Figure 2, after cycling a surface layer deposited on top of titania nanotubes appears, which may be the residual electrolyte salt after sample cleaning. The stable reversible capacity and stable cyclability of titania nanotube may be attributed to two features of the films: the intrinsic low volume expansion of titania during lithium-ion insertion and extraction[7] and the hollow structure of titania nanotubes which accommodates volume expansion and DISs, which will be discussed later.

An important factor that limits the application of bulk TiO_2 polymorphs as LIB electrodes is the low Li$^+$-ion diffusion rate and low electrical conductivity of TiO_2. With a nanotube structure composed of thin walls, the diffusion distance is sharply decreased and both lithium diffusion and electrical conductivity become less of a limitation. The capacity differences among titania films prepared under different voltages is primarily due to the variation of thickness and porosity of the film. Comparing samples obtained at anodization voltages of 10 and 20 V, the porosity does not change much but the thickness increases from 350 to 550 nm. As the pores go deeper, it is reasonable that more material at the end of the pores remains less lithiated during cycling. Thus, the capacity of titania anodized at 20 V is smaller than that of 10 V. When the anodization voltage increased to 30 V, the titania is eroded at the top and the film thickness was reduced
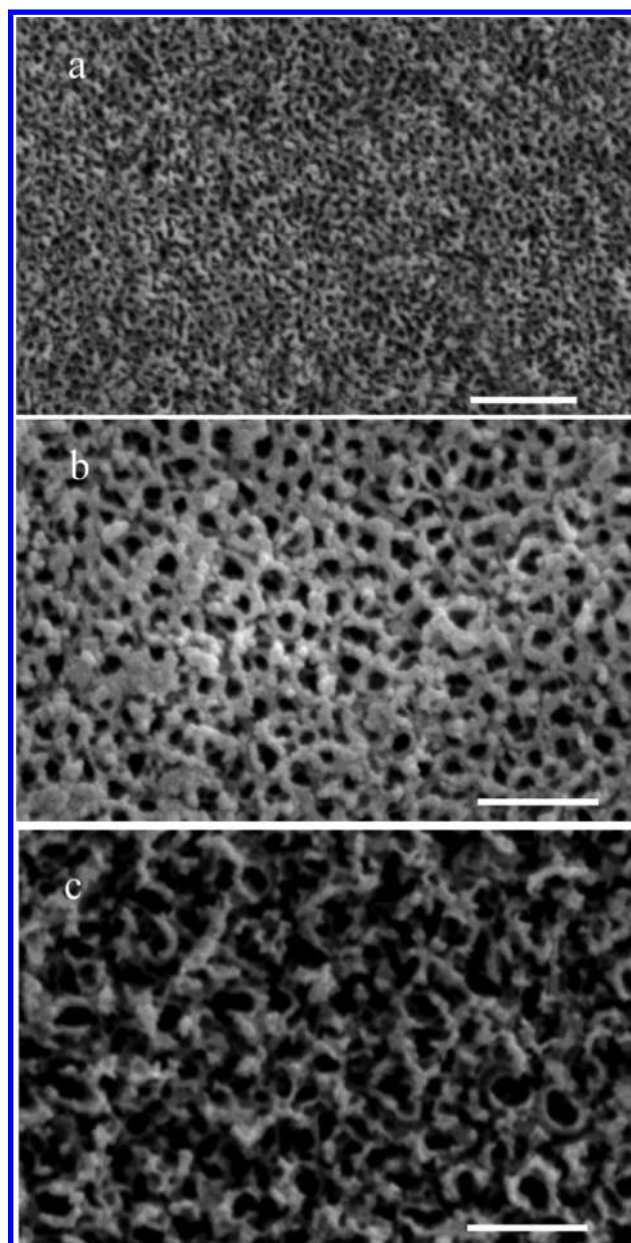
to 350 nm. Thus, more material is active in the electrochemical reactions.

3.3. Analysis of Fracture Tendency for TiO_2 Nanotubes.
Mechanical degradation, such as cracking and fracture of electrodes, is the main obstacle preventing commercial application of advanced LIB electrodes. Lithium diffusion into electrode materials results in diffusion-induced stresses (DISs), which cause mechanical degradation of the electrode materials and lead to loss of electric conduction. Recent publications utilized the analogy between thermal stresses and DISs to calculate the stress field evolution during electrochemical cycling.[33] In order to understand the good cycling performance of titania nanotubes observed in this work, we use a similar approach to calculate DISs in LIB electrode elements with cylindrical/tubular geometry. This analysis can be applied to other LIB electrode materials.

For cylindrically symmetric tubes with an inner radius of a and outer radius of R, the concentration of Li atoms at a particular position and time can be defined with the diffusion equation in a cylindrical coordinate system by

$$\frac{\partial C}{\partial t} = D\left(\frac{\partial^2 C}{\partial r^2} + \frac{1}{r}\frac{\partial C}{\partial r}\right) \tag{1}$$

where C is the molar concentration of Li and D is the Li diffusion coefficient inside the electrode material. We assume that constant flux diffusion occurs at the inner surface of the tubes, which represents constant current cycling in this work and the case of small modified Biot number under constant potential conditions,[34] and that there is no flux of Li from the outer surface. While there are small gaps indicated between some of the tubes in Figure 2, this is a reasonable assumption for nanotube arrays since the majority of the available surface area is at the inner tube surface. Hence, the boundary conditions of diffusion are

$$C(r, 0) = C_0, \text{ for } a \leq r \leq R \tag{1a}$$

$$D\frac{dC(r, t)}{dr}\bigg|_{r=a} = \frac{I}{F}, \text{ for } t \geq 0 \tag{1b}$$

$$D\frac{dC(r, t)}{dr}\bigg|_{r=R} = 0, \text{ for } t \geq 0 \tag{1c}$$

where F is Faraday's constant. Equation 1 can be transferred to dimensionless form with the definitions $x = r/R$, $\tau = (Dt)/R^2$, and $y = [C(r,t) - C_0][(FD)/(IR)]$. Calculation and discussion of DISs are given in Appendix A, Supporting Information.

During cracking, strain energy stored in materials is transferred to the surface energy associated with generated cracks. Following Cheng and Verbrugge,[35] the bulk strain energy density, $e(r)$, accumulated as a result of elastic deformation of the isotropically deformed tube, can be calculated as

$$e(r) = \frac{1}{2E}(\sigma_r^2 + \sigma_\theta^2 + \sigma_z^2) - \frac{\nu}{E}(\sigma_r\sigma_\theta + \sigma_\theta\sigma_z + \sigma_z\sigma_r) \tag{2}$$

where σ_i represents the principle stress in coordinate "i" of a cylindrical coordinate system. E and ν are the Young's modulus and Poisson's ratio of the electrode material, respectively. The total bulk strain energy can be obtained by integrating the strain energy density over the entire volume.

$$E_{\text{bulk}} = \int_a^R e(r)\cdot h\cdot r\, dr \tag{3a}$$

The bulk strain energy of the tube in dimensionless form (Π_{strain}) is

$$\Pi_{\text{strain}} = \frac{E_{\text{bulk}}}{E\pi R^2 h\left(\frac{\Omega}{3(1-\nu)}\frac{IR}{FD}\right)^2}$$
$$= \int_{(a/R)}^1 [(\xi_r^2 + \xi_\theta^2 + \xi_z^2) - 2\nu(\xi_r\xi_\theta + \xi_\theta\xi_z + \xi_z\xi_r)]x\, dx \tag{3b}$$

where E_{bulk} is the strain energy, Ω the coefficient of the volume expansion per mole of lithium, and $\xi_i = \sigma_i/([(\Omega/3)(E/(1-\nu))((IR)/(FD))])$ is the dimensionless stress.

For a crack to propagate, the fracture energy E_f should exceed the surface energy of newly created cracks, i.e.

$$E_f = \gamma_{\text{surface}}\cdot A_s \tag{4}$$

Here γ is the surface energy per unit area, and A_s is the area of new surfaces. If the fracture is a result of tangential/hoop stress, we assume that a crack of height h along the axial direction is created (Figure 8). We call such cracking "tangential cracking". The fracture energy for such a crack is

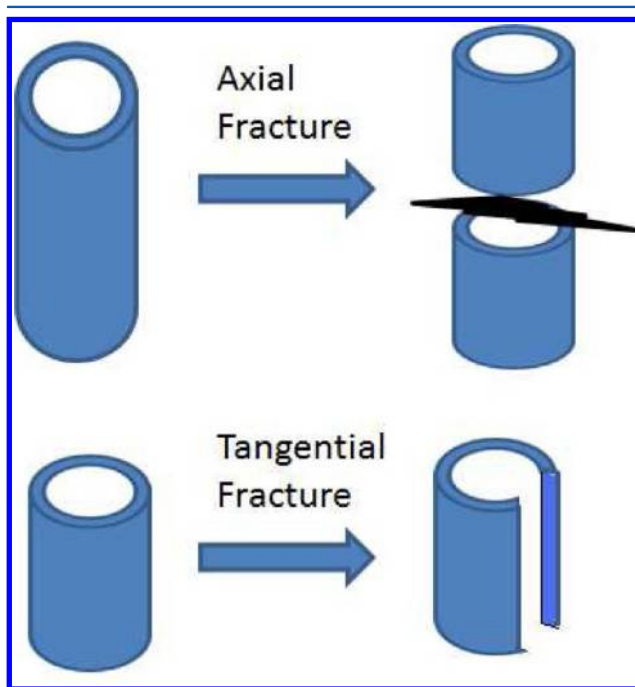$$E_{f,\text{tan gential}} = \gamma_{\text{surface}}\cdot 2(R - a)h \tag{5}$$

Figure 8. Schematic illustrating tubular electrode undergoing axial and tangential fracture during charge/discharge operation.

Similarly, if the fracture is a result of axial stress, we assume that the tube is broken into two pieces, each with a length smaller than the original value (Figure 8). We call such cracking "axial cracking". Fracture energy in this case is given by

$$E_{f,\text{axial}} = \gamma_{\text{surface}}\cdot 2\pi(R^2 - a^2) \tag{6}$$

The fracture energy can be normalized with a parameter similar to what we used for the bulk strain energy (in eq 3b)

$$\Pi_{\text{fracture}} = \frac{E_f}{E\pi R^2 h\left(\frac{\Omega}{3(1-\nu)}\frac{IR}{FD}\right)^2} \tag{7}$$

The fracture tendency can be defined as the ratio between the maximum strain energy and fracture energy[36] as

$$\text{Fracture tendency} = \frac{\text{Stored strain energy}}{\text{fracture energy required}} = \frac{\Pi_{\text{strain}}}{\Pi_{\text{fracture}}} \tag{8}$$

If the fracture energy required for axial cracking is less than that required in tangential cracking, the tube would be more prone to axial cracking than tangential cracking and vice versa. The effect of fracture tendency on cracking can be divided into two categories depending upon the length of the tube.

Case 1: Long tubes; i.e., $h > (R + a)$. Relatively long tubes are more prone to axial cracking. The axial fracture energy is normalized as

$$
\begin{aligned}
\prod\nolimits_{\text{f,axial}} &= \frac{\gamma_{\text{surface}} \cdot 2\pi (R^2 - a^2)}{E \pi R^2 h \left(\frac{\Omega}{3(1-\nu)} \frac{IR}{FD} \right)^2} \\
&= \frac{2\gamma_{\text{surface}}}{E \left(\frac{\Omega}{3(1-\nu)} \frac{IR}{FD} \right)^2} \frac{1}{h} \left(1 - \frac{a^2}{R^2} \right) \\
&= \frac{K}{I^2 (R)^2} \frac{1}{h} \left(1 - \frac{a^2}{R^2} \right)
\end{aligned}
\tag{9}
$$

Here we define $K \equiv (2\gamma_{\text{surface}})/((E(\Omega/(3(1-\nu))(1/(FD))))^2)$, which is a constant for a specific material at a given current density. The dimensionless axial fracture energy depends on the current, the radius of the tube R, the length of the tube h, and the ratio a/R.

Case 2: Short tubes; i.e., $h < (R + a)$. Relatively shorter tubes are more prone to tangential cracking. The tangential fracture energy is normalized as

$$
\begin{aligned}
\prod\nolimits_{\text{f,tangential}} &= \frac{\gamma_{\text{surface}} \cdot 2(R - a) h}{E \pi R^2 h \left(\frac{\Omega}{3(1-\nu)} \frac{IR}{FD} \right)^2} \\
&= \frac{2\gamma_{\text{surface}}}{E \left(\frac{\Omega}{3(1-\nu)} \frac{IR}{FD} \right)^2} \frac{1}{\pi R} \left(1 - \frac{a}{R} \right) \\
&= \frac{K}{I^2} \frac{1}{\pi R^3} \left(1 - \frac{a}{R} \right)
\end{aligned}
\tag{10}
$$

The dimensionless fracture energy depends on the current, the radius of the tube R, as well as the ratio a/R but is independent of the tube length h.

Between these two modes of cracking, axial cracking might be more detrimental to LIB electrodes, since it leads to the loss of electrical conduction by the electrodes and thus results in capacity fading. On the other hand, pure tangential (hoop) cracking results in opening up of the tube with two parts which may retain contact with the substrate/current collector (Figure 8). Electrode materials are active during the following cycling, and capacity retention is not affected by tangential cracking.

In the current work, titania nanotubes with three different dimensions are studied, whose outer radii are 32, 53, and 70 nm and tube lengths are 355, 540, and 351 nm, respectively. For all three cases, the tubes are more prone to axial fractures, i.e., they fall within Case 1 above. The tube length is large enough that we can neglect the end effects from the substrate. DIS evolution in these tubes is modeled with generalized plane strain conditions. We assume that the electrode material is an isotropic, linearly elastic solid. Using the analogy between thermal stresses[35,37] and DISs,[38] the stress−strain relationships for the radial, tangential, and axial components can be calculated (Appendix A, Supporting Information).

Fracture tendencies of titania nanotubes are calculated using eqs 3a and 3b and 8−10. The local current density of TiO_2 nanotubes in this work is 6.2×10^{-3}, 5.1×10^{-3}, and 13×10^{-3} mA cm^{-2} for anodization at 10, 20, and 30 V, respectively (see Appendix B, Supporting Information). The diffusion coefficient of lithium inside TiO_2 tubes[39] is 2×10^{-8} m^2 s^{-1}. We find that the values of fracture tendencies for titania nanotubes during

electrochemical cycling are calculated to be 4.9×10^{-9}, 5.2×10^{-9}, and 7.5×10^{-8}. These values are extremely small compared to the values of fracture tendencies reported for nanowires in Deshpande et al.,[36] which were on the order of 10^{-2} for different materials. It is reasonable to conclude based on these calculations that there is little probability for cracking to occur during cycling. Thus, it is not surprising that titania nanotubes in this work show good capacity retention and stable cycling performance.

3.4. Designing Nanotube Electrodes Based on DIS and Fracture Tendency. The geometry of nanotubes, including the length and outer and inner radii, affects the fracture tendency strongly. Fracture tendencies for titania nanotubes during delithiation for different a/R ratios of tubes and fixed tube length and local current densities (1 mA cm^{-2}) are compared in Figure 9a. Solid lines represent the tangential fracture tendency, and dashed lines represent the axial fracture tendency. It is seen that both tangential and axial fracture
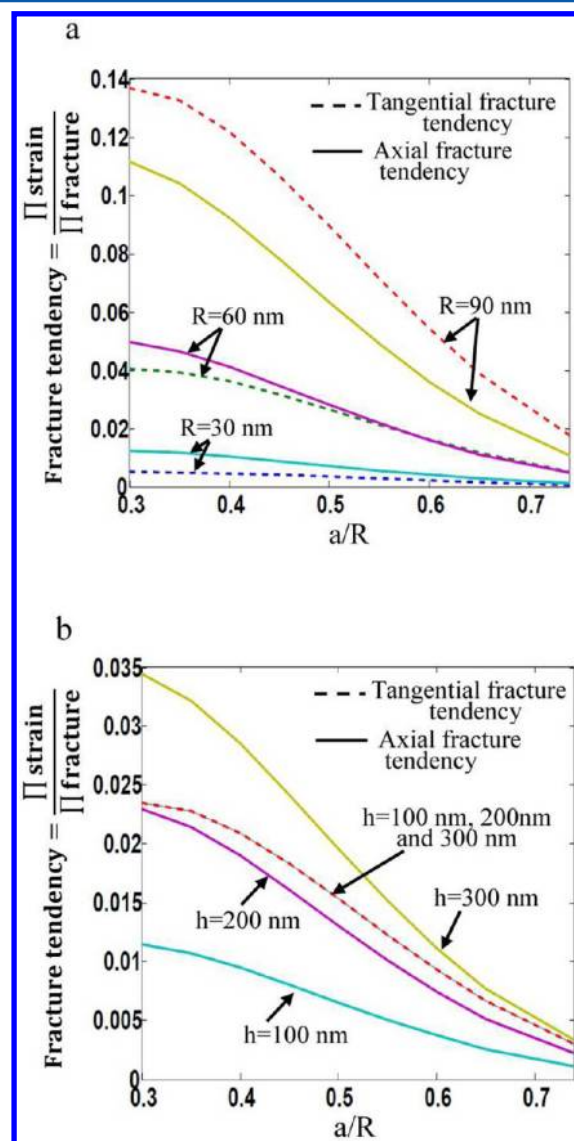

Figure 9. Fracture tendency as a function of the ratio of the inner radius to the outer radius of tubes (a/R) assuming current density $I = 1$ mA cm^{-2} and (a) height of the tube fixed at $h = 300$ nm or (b) radius of the tube fixed at $R = 50$ nm.

tendencies decrease with an increase in the a/R ratio and that the nanotube electrodes are less prone to mechanical degradation. However, large a/R is equivalent to small tube thickness and subsequently a small amount of active material per unit volume of electrode. On the other hand, a small a/R ratio (a/R close to 0) gives a denser film of active materials; the effect of axial diffusion in terms of stresses is strong. Diffusion boundary conditions are changed, and DISs and fracture tendencies are different from the current case. At the same time, an increase in a/R leads to a decrease in active material volume fraction in the electrodes and thus a decrease in volumetric energy density.

Also, for a given a/R ratio of the tube, as the outer radius increases, both fracture tendencies increase (Figure 9a). At the same time, smaller tube diameter implies small diffusion length and in turn better battery power. Thus, the porosity of TiO_2 nanotube electrodes can be tuned with dimensions falling into a "safe" region.

The effect of tube lengths on fracture tendencies for a nanotube with fixed radius is plotted in Figure 9b. In agreement with eqs 5 and 10, the tangential fracture energy is found to be independent of tube length; at the same time, axial fracture tendency increases with increasing tube length. Thus, short tubes are less prone to cracking. In LIBs, fracture tendencies should be much smaller than 1 for stable cycling performance. In the mean time, dense and long tubes provide large charge and energy density of LIB electrodes.

In addition to the dimensions of the tube, the cracking tendency is also related to the current density during charging and discharging (eqs 9 and 10). We define the critical current density as the current density at which the fracture tendency reaches unity. We estimate the current densities for the tubes to be approximately 6.2×10^{-3}, 5.1×10^{-3}, and 13×10^{-3} mA cm^{-2} for tubes prepared at 10, 20, and 30 V, respectively (Appendix B, Supporting Information). The critical current densities required for a crack to appear are 9.6, 7.1, and 4.7 mA cm^{-2}, respectively. Thus, the current densities used in the experiments are much lower than the critical values and give low fracture tendencies, and the materials are stable upon electrochemical cycling, leading to high capacity retention.

The effect of current density on the fracture tendency is plotted in Figure 10 for a representative tube geometry (height h = 351 nm, radius r = 50 nm, and a/R = 0.5). For nanotubes with any given geometry, fracture tendency increases with an increase in current density. The value of critical current density decreases with increasing radius of the tubes. For the given example the fracture tendency exceeds unity at a current density of 6.7 mA cm^{-2}. The local current density depends upon the surface area of tubes available for diffusion of lithium and thus the surface roughness. For increased local current density, for example, 2 mA cm^{-2}, the fracture tendencies are less than 0.1 and it is reasonable to expect that titania will not suffer mechanical degradation. Thus, the cycling performance of titania nanotubes will still be good, even at higher current density or higher cycling rates than what was used in these experiments. However, effects from lithium diffusion, polarization, and side reactions should be considered when setting charging and discharging rates and current densities.

4. CONCLUSIONS

Vertically aligned amorphous titania nanotubes with tunable inner pore diameter and wall thickness were fabricated by anodization of Ti foils at various voltages. The pore diameter
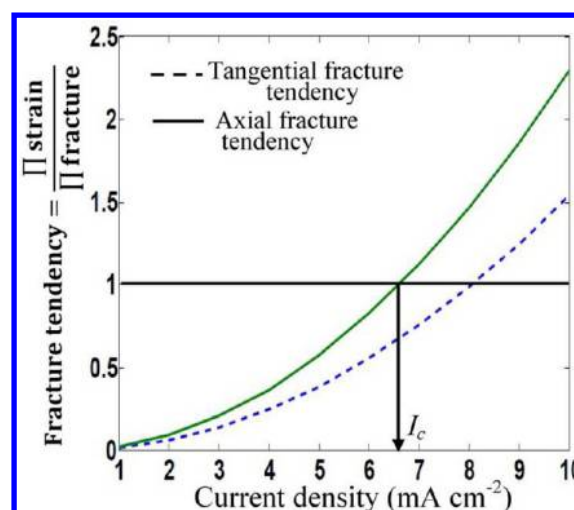

Figure 10. Fracture tendency as a function of current density for a given set of dimensions of the tube. Solid line represent tangential fracture tendency, and dashed line represents axial fracture tendency.

and wall thickness of titania nanotubes varied from 30 to 70 nm and 17 to 35 nm, respectively. The fabricated titania nanotubes were employed as negative electrodes for lithium-ion batteries. Titania remained amorphous during electrochemical cycling and remained in contact with the substrate after cycling. Titania nanotube arrays present good cycling behavior, with capacities between 150 and 230 mAh g^{-1} and little drop in capacity up to 200 cycles. From SEM observation, no cracks are found on the surface of titania nanotubes after 200 cycles and the nanotube morphology is retained.

On the basis of simulated fracture tendencies derived from the diffusion-induced stress (DIS) model, electrodes with hollow tubular structures are more prone to cracking during delithiation than the lithiation process due to the much higher tangential stresses encountered during delithiation. All stresses including radial, tangential, and axial stress can be reduced by decreasing the wall thickness of tubes. Consistent with this, both tangential and axial fracture tendencies decrease with an increasing ratio of the inner to the outer radius of tubes regardless of the length and radius of tubes. Furthermore, for tubes with the same length, increasing the radius causes the axial fracture tendency (which is proportional to the radius and length of the tubes) to transfer from higher to lower than the tangential fracture tendency (which is proportional to the radius and independent of the length of the tubes). These properties allow tubular materials with thin wall to be outstanding candidates for electrodes in lithium-ion batteries.

In addition to the titania nanotubes synthesized here, the approach presented is to calculate the mechanical properties of electrodes based on the DIS model initiated from dimensionless analysis and therefore is applicable to other electrode materials with tubular structures. The principle demonstrated here of using tubular electrode arrays with thin wall to find the optimal structure balancing high volumetric capacity and long cycling life should be of great significance for the design of lithium-ion batteries with superior electrochemical performance.

■ ASSOCIATED CONTENT

S Supporting Information

Appendix A, describing the calculation of diffusion-induced stresses, and Appendix B, showing a sample calculation of current density. This material is available free of charge via the Internet at http://pubs.acs.org.

■ AUTHOR INFORMATION

Corresponding Author

*E-mail: srankin@engr.uky.edu (S.E.R.); fyang0@engr.uky.edu (F.Y.); ycheng@engr.uky.edu (Y.-T.C.).

Present Addresses

[‡]Chemical Sciences and Engineering Division, Argonne National Laboratory, 9700 South Cass Avenue, Argonne, Illinois 60439, United States.

[⊥]Materials Science and Technology Division, Oak Ridge National Laboratory, 1 Bethel Valley Dr., Oak Ridge, TN 37830, United States.

[§]Lawrence Berkeley National Laboratory, Mail Box 70R0108B, 1 Cyclotron Road, Berkeley, California 94720, United States.

[∥]Laboratory of Energy and Nano Science (LENS), Materials Science and Engineering, Masdar Institute of Science and Technology (MIST), P.O. Box 54224, Abu Dhabi, United Arab Emirates.

Author Contributions

[†]These authors contributed to this work equally.

Notes

The authors declare no competing financial interest.

■ ACKNOWLEDGMENTS

■ REFERENCES

(1) Xu, T.; Wang, W.; Gordin, M. L.; Wang, D.; Choi, D. *J. Mater.* **2010**, *62*, 24.

(2) Park, C.-M.; Kim, J.-H.; Kim, H.; Sohn, H.-J. *Chem. Soc. Rev.* **2010**, *39*, 3115.

(3) Winter, M. Z. *Phys. Chem., Int. J. Res. Phys. Chem. Chem. Phys.* **2009**, *223*, 1395.

(4) Scrosati, B.; Garche, J. *J. Power Sources* **2010**, *195*, 2419.

(5) Ortiz, G. F.; Hanzu, I.; Djenizian, T.; Lavela, P.; Tirado, J. L.; Knauth, P. *Chem. Mater.* **2009**, *21*, 63.

(6) Wang, D.; Choi, D.; Yang, Z.; Viswanathan, V. V.; Nie, Z.; Wang, C.; Song, Y.; Zhang, J.-G.; Liu, J. *Chem. Mater.* **2008**, *20*, 3435.

(7) Wagemaker, M.; Kearley, G. J.; van Well, A. A.; Mutka, H.; Mulder, F. M. *J. Am. Chem. Soc.* **2003**, *125*, 840.

(8) Yang, Z.; Choi, D.; Kerisit, S.; Rosso, K. M.; Wang, D.; Zhang, J.; Graff, G.; Liu, J. *J. Power Sources* **2009**, *192*, 588.

(9) Tang, Y.; Yang, L.; Qiu, Z.; Huang, J. *J. Mater. Chem.* **2009**, *19*, 5980.

(10) Liu, Z.; Hong, L.; Guo, B. *J. Power Sources* **2005**, *143*, 231.

(11) Armstrong, A. R.; Armstrong, G.; Canales, J.; Garcia, R.; Bruce, P. G. *Adv. Mater.* **2005**, *17*, 862.

(12) Lindsay, M. J.; Blackford, M. G.; Attard, D. J.; Luca, V.; Skyllas-Kazacos, M.; Griffith, C. S. *Electrochim. Acta* **2007**, *52*, 6401.

(13) Lindsay, M. J.; Skyllas-Kazacos, M.; Luca, V. *Electrochim. Acta* **2009**, *54*, 3501.

(14) Fang, H.-T.; Liu, M.; Wang, D.-W.; Sun, T.; Guan, D.-S.; Li, F.; Zhou, J.; Sham, T.-K.; Cheng, H.-M. *Nanotechnology* **2009**, *20*, 225701/1.

(15) Wei, Z.; Liu, Z.; Jiang, R.; Bian, C.; Huang, T.; Yu, A. *J. Solid State Electrochem.* **2010**, *14*, 1045.

(16) Gong, D.; Grimes, C. A.; Varghese, O. K.; Hu, W.; Singh, R. S.; Chen, Z.; Dickey, E. C. *J. Mater. Res.* **2001**, *16*, 3331.

(17) Cai, Q.; Paulose, M.; Varghese, O. K.; Grimes, C. A. *J. Mater. Res.* **2005**, *20*, 230.

(18) Macak, J. M.; Tsuchiya, H.; Taveira, L.; Aldabergerova, S.; Schmuki, P. *Angew. Chem., Int. Ed.* **2005**, *44*, 7463.

(19) Furukawa, H.; Hibino, M.; Honma, I. *J. Electrochem. Soc.* **2004**, *151*, A527.

(20) Cheng, Y.-T.; Verbrugge, M. W. *J. Power Sources* **2009**, *190*, 453.

(21) Cheng, Y.-T.; Verbrugge, M. W. *J. Appl. Phys.* **2008**, *104*, 083521.

(22) Verbrugge, M. W.; Cheng, Y.-T. *J. Electrochem. Soc.* **2009**, *156*, A927.

(23) Deshpande, R.; Cheng, Y.-T.; Verbrugge, M. W. *J. Power Sources* **2010**, *195*, 5081.

(24) Yang, F. *Mater. Sci. Eng., A* **2005**, *409*, 153.

(25) Yang, F. Q. *J. Appl. Phys.* **2010**, *108*.

(26) Mor, G. K.; Varghese, O. K.; Paulose, M.; Mukherjee, N.; Grimes, C. A. *J. Mater. Res.* **2003**, *18*, 2588.

(27) Hassan, F. M. B.; Nanjo, H.; Tetsuka, H.; Kanakubo, M.; Aizawa, T.; Nishioka, M.; Ebina, T.; Bond, A. M. *J. Electrochem. Soc.* **2009**, *156*, K227.

(28) Macdonald, D. D. *J. Electrochem. Soc.* **1993**, *140*, L27.

(29) Mor, G. K.; Varghese, O. K.; Paulose, M.; Shankar, K.; Grimes, C. A. *Sol. Energy Mater. Sol. Cells* **2006**, *90*, 2011.

(30) Kavan, L.; Kalbac, M.; Zukalova, M.; Exnar, I.; Lorenzen, V.; Nesper, R.; Graetzel, M. *Chem. Mater.* **2004**, *16*, 477.

(31) Baudrin, E.; Cassaignon, S.; Koelsch, M.; Jolivet, J. P.; Dupont, L.; Tarascon, J. M. *Electrochem. Commun.* **2007**, *9*, 337.

(32) Kavan, L.; Graetzel, M.; Gilbert, S. E.; Klemenz, C.; Scheel, H. J. *J. Am. Chem. Soc.* **1996**, *118*, 6716.

(33) Christensen, J.; Newman, J. *J. Electrochem. Soc.* **2006**, *153*, A1019.

(34) Cheng, Y.-T.; Verbrugge, M. W. *J. Electrochem. Soc.* **2010**, *157*, A508.

(35) Timoshenko, S.; Goodier, J. N. *Theory of elasticity*; McGraw-Hill: New York, 1951.

(36) Deshpande, R.; Qi, Y.; Cheng, Y.-T. *J. Electrochem. Soc.* **2010**, *157*, A967.

(37) Carslaw, H. S.; Jaeger, J. C. *Conduction of heat in solids*, 2nd ed.; Clarendon Press: Oxford, 1959.

(38) Prussin, S. *J. Appl. Phys.* **1961**, *32*, 1876.

(39) Zaghib, K.; Simoneau, M.; Armand, M.; Gauthier, M. *J. Power Sources* **1999**, *81−82*, 300.